

## Article

# SiO<sub>2</sub>-Alginate-Based Gel Polymer Electrolytes for Zinc-Ion Batteries

Peishu Tian <sup>1</sup>, Xin Zhong <sup>1</sup>, Caiting Gu <sup>1</sup>, Zhe Wang <sup>2</sup> and Fengwei Shi <sup>1,2,\*</sup>

<sup>1</sup> School of Chemical Engineering, Changchun University of Technology, Changchun 130012, China

<sup>2</sup> Key Laboratory of Advanced Functional Polymer Membrane Materials of Jilin Province, Changchun 130012, China

\* Correspondence: sfw0403@ccut.edu.cn

**Abstract:** Aqueous Zn-ion batteries (AZIBs) are quite promising energy sources. However, aqueous electrolytes present many challenges such as hydrolysis reactions, liquid leakage, Zn dendrites, and interfacial side reactions. To solve the above problems of aqueous electrolytes, in this study, a kind of SiO<sub>2</sub>-sodium alginate gel polymer electrolyte (SiO<sub>2</sub>-SA GPE) is prepared through a one-pot method. The SiO<sub>2</sub>-SA GPE possessed high ionic conductivity of  $1.144 \times 10^{-2} \text{ S}\cdot\text{cm}^{-1}$  and perfect mechanical strength. The Zn//LiFePO<sub>4</sub> batteries assembled with SiO<sub>2</sub>-SA GPE delivered a high discharge specific capacity of  $89.9 \text{ mAh g}^{-1}$  (capacity retention = 74.9%) after 300 cycles at 1 C, which was much better than traditional liquid electrolytes (residual discharge capacity =  $79.2 \text{ mAh g}^{-1}$ ). Results of the rate performance and long cycle life of AZIBs proved that SiO<sub>2</sub>-SA GPE could effectively prevent zinc dendrites and side reactions, providing a feasible strategy for improving the performance of AZIBs.

**Keywords:** aqueous zinc-ion batteries; sodium alginate; SiO<sub>2</sub>; gel polymer electrolytes; dendrite restriction



**Citation:** Tian, P.; Zhong, X.; Gu, C.; Wang, Z.; Shi, F. SiO<sub>2</sub>-Alginate-Based Gel Polymer Electrolytes for Zinc-Ion Batteries. *Batteries* **2022**, *8*, 175. <https://doi.org/10.3390/batteries8100175>

Academic Editor: Carlos Zieber

Received: 11 September 2022

Accepted: 29 September 2022

Published: 11 October 2022

**Publisher's Note:** MDPI stays neutral with regard to jurisdictional claims in published maps and institutional affiliations.



**Copyright:** © 2022 by the authors. Licensee MDPI, Basel, Switzerland. This article is an open access article distributed under the terms and conditions of the Creative Commons Attribution (CC BY) license (<https://creativecommons.org/licenses/by/4.0/>).

## 1. Introduction

The requirements of low-carbon emissions and exploring feasible sustainable patterns of living have become an imperative issue and attracted worldwide attention. With the rapid development of economic society, the consumption of energy is growing dramatically [1,2]. Renewable and green energies of nature, such as wind energy, solar energy, and tidal energy, are encouraged powers, while the intermittence and dispersion of the above energies makes them difficult to meet the requirements for providing long-term and continuous supply for human society [3]. Therefore, electric energy storage has become the most reliable and practical energy storage method to date [4,5]. Among various fields, Li-ion batteries (LIBs) were used in a wide range of applications owing to their good cycle stability with high energy density [6–10]. Nevertheless, the limitations of LIBs have continuously become visible, such as insufficient reserves and the chemical instability of Li, pollution, and hidden safety hazards in the working process [11–16]. Therefore, safer, greener, and more efficient batteries are being actively researched and developed. With the advantages of high theoretical capacity ( $5855 \text{ mAh cm}^{-3}$ ), good stability, and low cost [17–20], aqueous zinc-ion batteries (AZIBs) have become one of alternatives to LIBs [21,22]. Notably, the aqueous electrolyte, compared with the traditional organic electrolyte, endows AZIBs with reliable safety [23]. Nonetheless, AZIBs still suffer from problems such as dendrite growth and aqueous electrolyte decomposition [24,25]. Effectively addressing these issues is an urgent issue and will enable the large-scale industrial application of zinc-ion batteries [26–28].

Recently, gel polymer electrolytes (GPEs) have been suggested to overcome the above challenges, and scientific research of GPEs based on ZIBs has been gradually developed [29]. Compared with liquid electrolyte (LE), GPEs can greatly reduce the water content but maintain dimensional stability [30]. At the same time, the contact surfaces between GPE

and electrodes are solid–solid surfaces, which can effectively inhibit dendrites and reduce the water-induced side reactions during the charge/discharge process [31,32].

In this paper, a novel GPE of organic–inorganic networks was fabricated by  $\text{SiO}_2$  and sodium alginate (SA), which possessed high ionic conductivity ( $1.144 \times 10^{-2} \text{ S}\cdot\text{cm}^{-1}$ ) and excellent mechanical properties. SA in this system cross-linked with divalent zinc ions, which could stabilize the polymer network structure and improve the mechanical properties of GPE [33,34]. Compared with LE, the inherent advantages of a GPE structure could slow down the tip effect, promote more efficient electrochemical processes, and show reversible electrochemical reaction kinetics [35,36]. Under the fixation of the three-dimensional skeleton structure of the polymer, the directional migration of zinc ions is guided rapidly, and the formation of zinc dendrites was suppressed [37]. The ion transport mechanism of prepared GPE was also studied, which could pave the way for the research and development of biomass-based electrolytes for ZIBs.

## 2. Experimental Section

### 2.1. Reagents and Materials

Sodium alginate (SA, AR), tetraethyl orthosilicate (TEOS, 98%), glycerol, LiFePO<sub>4</sub> (LFP, 98%), carbon black (CB, 98%), zinc chloride (ZnCl<sub>2</sub>, 98%), and lithium chloride (LiCl, 98%) were purchased from Aladdin (China). Hydrochloric acid (HCl, 37%) was obtained from Hisoar (Zhejiang, China). A GF separator was purchased from Whatman (Buckinghamshire, UK). All the reagents mentioned above can be used directly without further purification.

### 2.2. Preparation of the $\text{SiO}_2$ -SA GPE

$\text{SiO}_2$ - and SA-network hydrogel electrolyte ( $\text{SiO}_2$ -SA GPE) was prepared through the one-pot method. Figure 1 illustrates the schematic diagram of the preparation process of  $\text{SiO}_2$ -SA GPE. SA (3.0 g) and set amounts of tetraethyl orthosilicate (TEOS: 0, 4, 8, 12 and 16 mL) and glycerol (3.5 mL) were dispersed in 50 mL of deionized water in a three-neck flask at 60 °C with mechanical stirring, and the pH was adjusted to 3–4 with hydrochloric acid for 2 h. Glycerol was chosen as a plasticizer. The three-neck flask was then heated to 80 °C. The above reaction was continued for 2 h until the tetraethyl orthosilicate hydrolyzed and the byproduct evaporated completely. Finally, the mixture was poured into a polytetrafluoroethylene mold and placed for 24 h to obtain the  $\text{SiO}_2$ -SA gel matrix. The substrate was immersed into the well-mixed salt solution that consisted of 5 mol·L<sup>-1</sup> ZnCl<sub>2</sub> and 4 mol·L<sup>-1</sup> LiCl to obtain  $\text{SiO}_2$ -SA GPE. The prepared GPEs were labeled as GPE 3-x, where x = 0, 4, 8, 12, and 16 represented the amount of TEOS, which was 0, 4, 8, 12, and 16 mL, respectively.

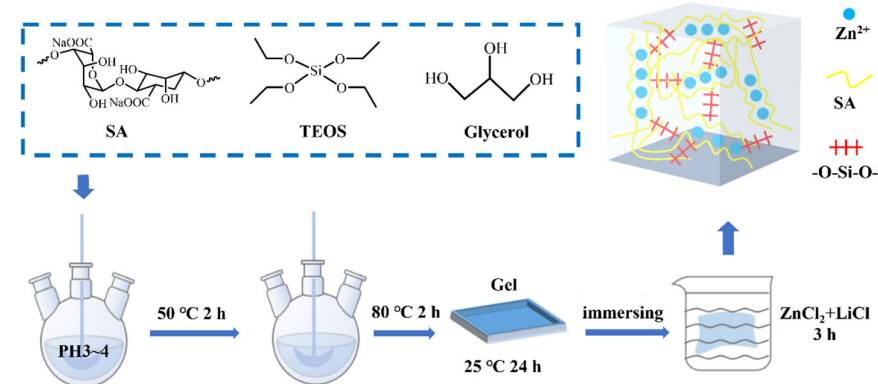


**Figure 1.** Schematic diagram of the preparation of  $\text{SiO}_2$ -SA GPE.

### 2.3. Battery Assembling

The quasi-solid Zn//LiFePO<sub>4</sub> batteries (CR2032 button-type cells) were assembled with the LiFePO<sub>4</sub> (LFP) cathode, prepared GPE, and Zn foils, in which the LFP cathode

was prepared following previous work [38]. For comparison, Zn//LFP batteries with LE were also prepared with LFP cathodes, GF paper separator,  $5 \text{ mol}\cdot\text{L}^{-1}$   $\text{ZnCl}_2$  and  $4 \text{ mol}\cdot\text{L}^{-1}$   $\text{LiCl}$  aqueous electrolyte, and Zn anodes. The cells were labeled as LFP/GPE/Zn and LFP/LE/Zn, respectively.

#### 2.4. Material Characterization

The samples were investigated by Fourier transform infrared spectroscopy (FT-IR-Nicolet/IS 50, Thermo Fisher Scientific, Waltham, MA, USA) within the wavenumber range of  $4000\text{--}400 \text{ cm}^{-1}$  to analyze the chemical component of GPEs. The Zn anode were performed by the X-ray diffraction (XRD) in the  $2\theta$  range of  $5\text{--}80^\circ$  (Rigaku Smart Lab, Tokyo, Japan, Cu target X-ray). Thermal gravimetric (TG) analysis measurements were performed on a STA6000 synchronous thermal analyzer (PerkinElmer, Waltham, MA, USA) in a nitrogen atmosphere ( $10 \text{ }^\circ\text{C min}^{-1}$ ). The morphologies and elemental distribution of the GPEs were investigated using a JSM-7610F emission scanning electron microscope (JEOL, Tokyo, Japan) equipped with an energy-dispersive spectroscopy detector (EDS). The AGS-X universal stretching machine of Shimadzu Corporation of Japan tested the tensile strength of the prepared GPE membrane (dumbbell-shaped sample, length 40 mm, width 4 mm, and thickness 0.5 mm).

#### 2.5. Electrochemical Characterization

AC impedance, linear scanning voltammetry (LSV), and cyclic voltammetry (CV) were carried out by an electrochemical workstation (CHI 660E, Chenhua Instrument Co., Ltd., Shanghai, China). The cycle stability and rate performance were examined by a Land-CT2001A battery tester (Wuhan, China). The C rates were calculated based on the equation:  $I = m_{\text{LiFePO}_4} \times C_{\text{LiFePO}_4} \times C$ , where  $I$  represented the value of constant charge/discharge current;  $m_{\text{LiFePO}_4}$  represented the weight of active substance; and  $C_{\text{LiFePO}_4}$  represented theoretical capacity of  $\text{LiFePO}_4$ . The EIS spectra were performed at a frequency range of  $10^{-2}\text{--}10^5 \text{ kHz}$ . In the LSV test, Ti foil was the working electrode, and Zn foils were utilized as the counter and reference electrodes.

### 3. Results and Discussion

As shown in Figure 2a, the influence of different volumes of TEOS on the  $\text{SiO}_2$ -SA GPE structure was investigated by FT-IR. The broad band at  $3300 \text{ cm}^{-1}$  was attributed to the O-H stretching vibration in the polymer chains of SA. The bands located at about  $1612 \text{ cm}^{-1}$  and  $1410 \text{ cm}^{-1}$  were assigned to the -COO- asymmetric stretching vibration and symmetric stretching vibration in the alginate chains [39]. After the addition of TEOS, two new peaks were found at  $921 \text{ cm}^{-1}$  and  $846 \text{ cm}^{-1}$ , which belonged to the stretching vibration of Si-OH and symmetric stretching vibration of -O-Si-O-, respectively [40]. Results indicated that TEOS had hydrolyzed and produced -O-Si-O-. The interaction might be formed through a hydrogen bond between -O-Si-O- and SA [41]. Figure 2b shows the cross-section of GPE, where a regularly arranged layer-by-layer structure was found. As demonstrated in the surface morphology (Figure 2c), GPE had multiple holes that promote the transport of  $\text{Zn}^{2+}$  ions and endow GPE with excellent ionic conductivity. On the EDS element maps of GPE (Figure 2d), the four elements of C, O, Na, and Si in the GPE matrix were distributed uniformly. It was indicated that -O-Si-O- interacted with SA, and the GPE hydrogel matrix was successfully prepared.

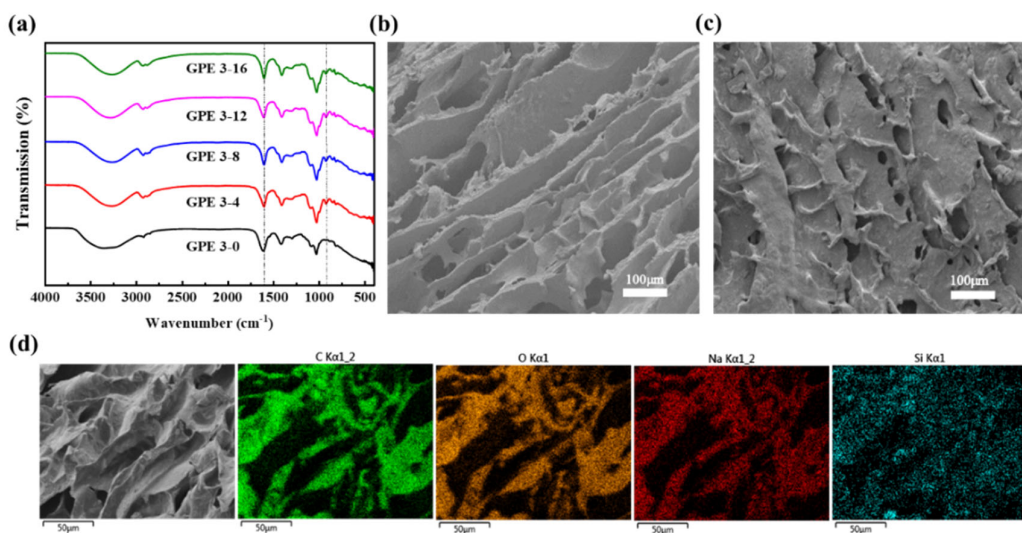


**Figure 2.** (a) FT-IR spectra of  $\text{SiO}_2$ -SA GPE; SEM images of GPE (b) cross-section and (c) surface; (d) EDS element maps of GPE.

The TG thermograms of the  $\text{SiO}_2$ -SA gel matrix are shown in Figure 3a. The weight loss of all samples caused by the evaporation of free water in the aerogel structure was within 5% between 0 °C and 150 °C. From 150 °C to 300 °C, the weight loss of gels decreased rapidly, which was due to the cleavage of the SA glycosidic bond [42]. It could be found that  $\text{SiO}_2$  had better thermal stability because the more  $\text{SiO}_2$  in gels, the more stable the gel. A gradual decrease in weight loss could be clearly observed above 300 °C, which might be due to the -O-Si-O- bond. From the DTA spectrum (Figure 3b), it could also be noticed that the peaks of the  $\text{SiO}_2$ -SA gel matrix became narrower and sharper, indicating that the matrix could transfer heat well.

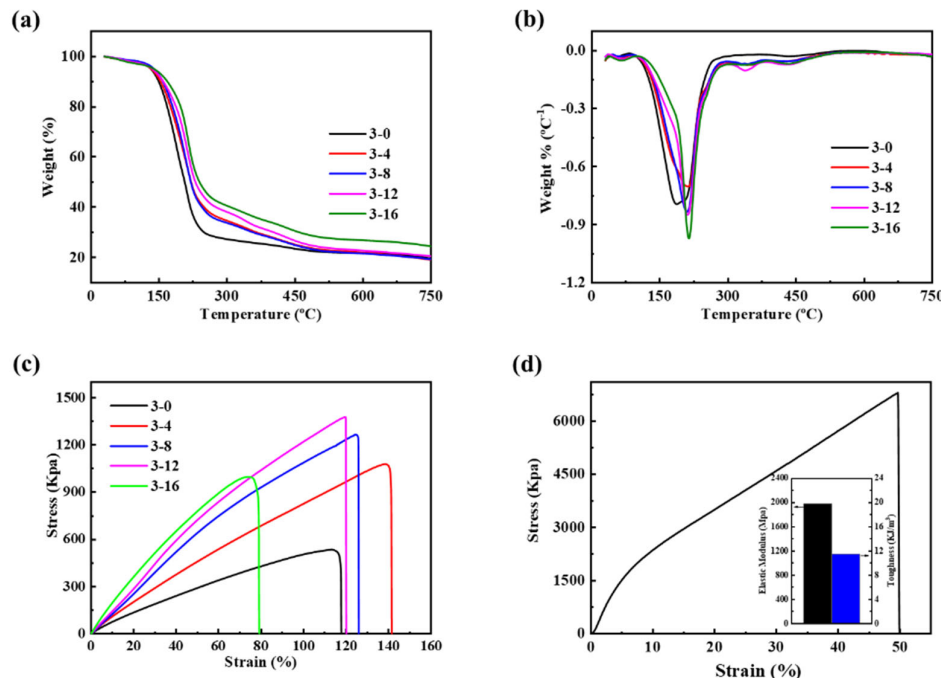


**Figure 3.** The (a) TG and (b) DTA curves of GPE; (c) stress-strain curves of GPE; (d) Stress-strain curves of GPE 3-12 after immersed in 5 mol  $\text{L}^{-1}$   $\text{ZnCl}_2$  and 4 mol  $\text{L}^{-1}$   $\text{LiCl}$ .

The mechanical properties of  $\text{SiO}_2$ -SA gel were important as they directly affect the safety of batteries. As shown in Figure 3c, gels 3-12 possessed a high tensile strength of

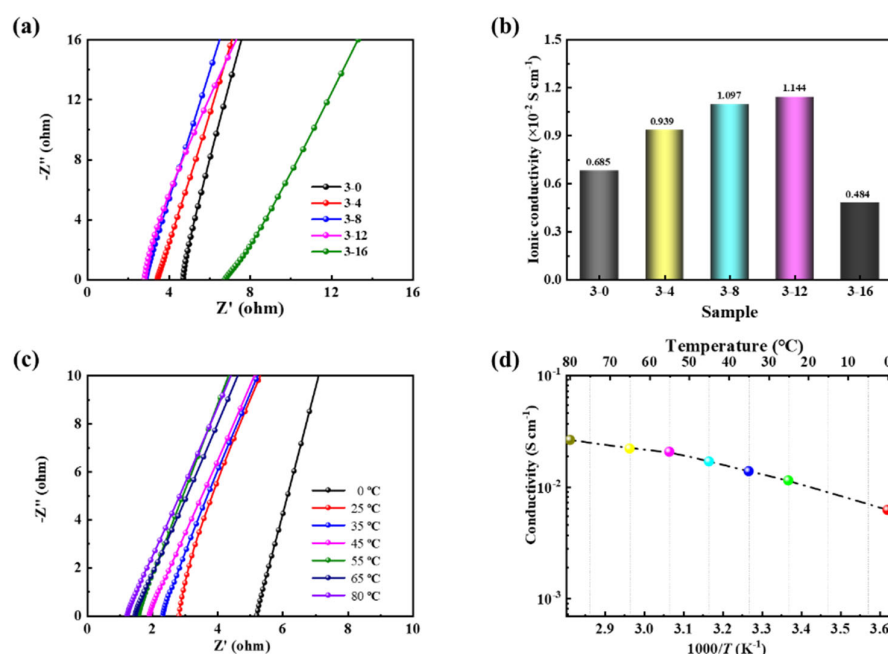
1380 KPa and relatively better fracture elongation of 120%. The tensile strength of gel 3-16 was lower than that of gel 3-12, which might be due to that the larger silica particles could be formed from excessive amounts of tetraethyl silicate hydrolysis, affecting the formation of the network structure and reducing the mechanical properties [39]. Gel 3-12 also exhibited high elastic modulus and toughness, as shown in Figure S1. The gel 3-12 soaked salt solution was used to obtain GPE 3-12, and its mechanical properties were tested. The GPE 3-12 tensile strength was significantly improved to 6800 KPa because of the cross-linking of zinc ions, and the modulus of elasticity and toughness also be increased (Figure 3d).

Figure 4a shows the AC impedance spectra of GPE with different TEOS contents at room temperature. As can be seen from the graph, the impedance of GPE decreased with the increasing TEOS content. However, the internal resistance of GPE suddenly increased when the ratio of SA to TEOS turned to 3-16, which might be due to the excessive -O-Si-O-networks. The ionic conductivity of GPE was calculated by:

$$\sigma = \frac{l}{RA}$$

where  $l$  was the thickness of the GPE (cm),  $R$  was the body resistance ( $\Omega$ ),  $A$  was the area of contact surface between the electrode material and GPE ( $\text{cm}^2$ ), and  $\sigma$  was the ion conductivity ( $\text{S}\cdot\text{cm}^{-1}$ ) [43]. The corresponding ionic conductivity is shown in Figure 4b. The changes in ionic conductivity and internal resistance of GPE showed the opposite trends. The ionic conductivity of GPE 3-12 is  $1.144 \times 10^{-2} \text{ S}\cdot\text{cm}^{-1}$ , which is larger than that of GPE 3-10 ( $1.097 \times 10^{-2} \text{ S}\cdot\text{cm}^{-1}$ ) and GPE 3-16 ( $0.484 \times 10^{-2} \text{ S}\cdot\text{cm}^{-1}$ ) owing to the appropriate three-dimensional hole structure of GPE 3-12. When the ratio of SA to TEOS increased to 3-16, the resistance of related samples increased, but the corresponding ionic conductivity decreased, which might be owing to the excessive networks blocking the ion transport channels. On the other hand, the lowest ionic conductivity of 3-16 mainly resulted from the excessive TEOS with the root cause that the inherent hydrophobic nature of Si–O–Si reduced the affinity between the  $\text{Zn}^{2+}$  ions and the hydrogel framework ions [44]. Results illustrated that the best ratio of SA to TEOS was 3-12, which was consistent with the results obtained by a stretching test. Therefore, the  $\text{SiO}_2$ -SA GPE prepared at the ratio of SA to TEOS of 3-12 was chosen for further investigation. Temperature has an important impact on battery performance. Extremely harsh temperature conditions can cause capacity decline and lifespan damage. Therefore, the impedance and ionic conductivity of GPE were studied at different temperatures (Figure 4c,d). When the temperature was changed from  $80^\circ\text{C}$  to  $0^\circ\text{C}$ , the ionic conductivity of GPE decreased from  $26.4 \times 10^{-2}$  to  $6.23 \times 10^{-2} \text{ mS}\cdot\text{cm}^{-1}$ . Both SA and silicone linkages was considered to possess good thermal stability of and the inherent anti-freeze resistance of glycerol and salt, which makes GPE have a wide range of temperature applications. Therefore, GPE still showed relatively stable electrochemical properties in extremely harsh environments [45].

The physical properties of  $\text{SiO}_2$ -SA GPE were studied and are shown in Figure 5. As illustrated, the thickness of the  $\text{SiO}_2$ -SA GPE was 0.58 mm (Figure 5a). It could be bent and folded at any angle and restored to its original shape (Figure 5b–e). It was commendable that after being made into thin strips (length of 60 mm and width of 4 mm), it could withstand a weight of 1 kg and be easily twisted without breaking (Figure 5f,g), indicating that the prepared GPE had excellent flexibility, strength, and toughness. The combustion test of GPE was further studied (Figure 5h). It showed that GPE cannot be burnt under open flame. After contacting with fire for 2 s and wiping the surface, GPE kept its morphology well. The stringent experiment was sufficient to demonstrate the excellent flame-retardant property of the prepared  $\text{SiO}_2$ -SA GPE to ensure the perfect safety of batteries.



**Figure 4.** (a) AC impedance spectra and (b) ionic conductivity of GPE; (c) AC impedance spectra and (d) ionic conductivity of GPE in different temperatures.

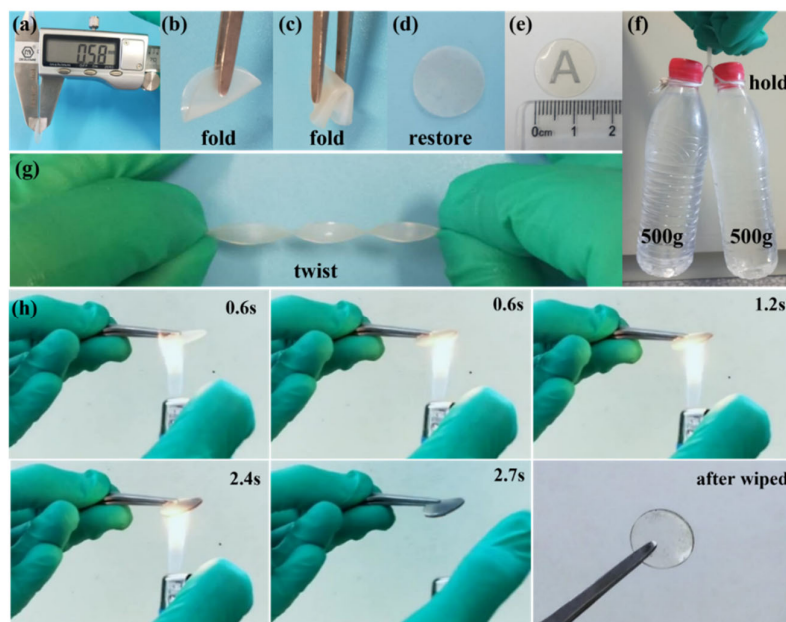


**Figure 5.** (a–g) Physical properties of GPE; (h) combustion experiments of GPE.

To examine the electrochemical properties of Zn/GPE/LFP cells, cyclic voltammetry (CV) measurements were performed at room temperature from  $0.1 \text{ mV s}^{-1}$  to  $2 \text{ mV s}^{-1}$ . The oxidation peak in the forward scan represented the release of lithium ions and the reduction peak in the reverse scan represented the insertion of lithium ions. As shown in Figure 6a,b, it could be seen that the CV curves in the two electrolyte systems were very similar, both exhibiting clear and distinct anodic and cathodic peaks, which proved the excellent chemical reversibility of the Zn/GPE/LFP hybrid batteries. The GPE demonstrated a total operating voltage window of 2.4 V (Figure 6d), which was broader than that of the LE (Figure 6c). Therefore, GPE can match almost all AZIBs [46–48].

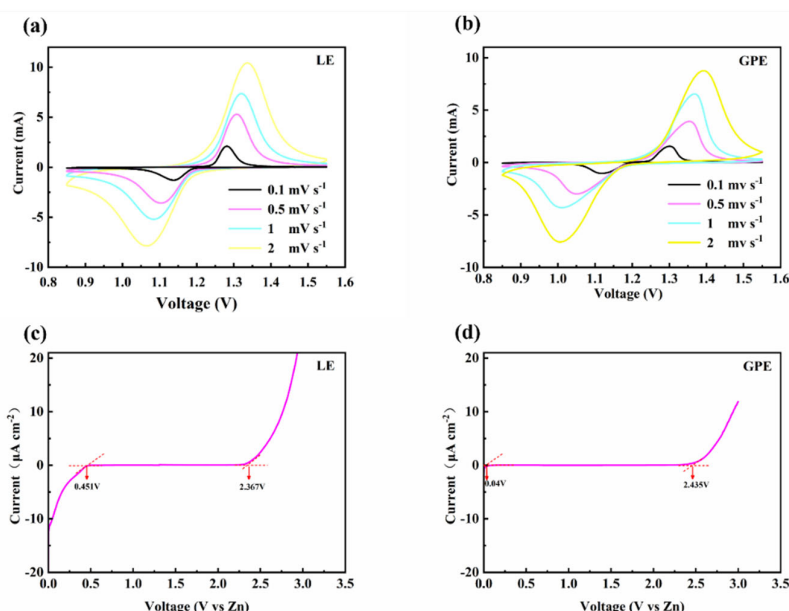


**Figure 6.** CV curves of (a) Zn/LE/LFP and (b) Zn/GPE/LFP at different scan rates; the electrochemical stability windows of (c) LE and (d) GPE.

The rate and cycling performance of Zn/LE/LFP and Zn/GPE/LFP were compared. Figure 7a depicts the rate performance of the Zn/LE/LFP cell, with initial specific capacities of 139.3, 127.0, 111.2, 86.8, and 75.7  $\text{mAh g}^{-1}$  at 0.5, 1, 2, 3, and 5 C, respectively. The corresponding charge/discharge profiles are showed at Figure S2. In contrast, the Zn/GPE/LFP cells showed superior rate performance with initial specific capacities of 140.8, 128.5, 112.1, 89.5, and 79.6  $\text{mAh g}^{-1}$  (Figure 7b), respectively. It was apparent that the capacity of GPE at each rate was higher than that of LE. When the current density returned to 0.5 C, the specific capacity of Zn/GPE/LFP immediately recovered close to the original value, reflecting the excellent rate performance. Figure 7c,d present the cyclability data of the Zn/LE/LFP and Zn/GPE/LFP rechargeable battery at 1 C (the initial three cycles were conducted at 0.2 C). The initial discharge capacity of the Zn/LE/LFP cell was 119.5  $\text{mAh g}^{-1}$  and the discharge capacity dropped to 79.2  $\text{mAh g}^{-1}$  with a capacity retention of only 66.3% after 300 cycles (Figure 7c). In contrast, the Zn/GPE/LFP cell had a similar initial capacity of 120.0  $\text{mAh g}^{-1}$  with the capacity retention rate of 74.9% after 300 cycles, and the Coulomb efficiency was close to 100% (Figure 7d). This result of stable electrochemical performance should be attributed to the mechanical inhibition of dendrites by GPE. With robust mechanical properties and stable pore structures, GPE could facilitate a homogeneous  $\text{Zn}^{2+}$  ion flow, leading to a uniform deposition of zinc metal and effective zinc dendrite prevention.

The galvanized charge/discharge method for Zn/Zn symmetric batteries was used to test the compatibility and stability of the electrolyte and metal anode. Figure 8a,b depict the voltage-time curves of Zn/LE/Zn and Zn/GPE/Zn cells at the current density of  $0.5 \text{ mA} \cdot \text{cm}^{-2}$  during 500 h for charge/discharge cycles. The polarization voltage of the Zn/LE/Zn cells increased slowly at 100 h and changed sharply after 155 h. On the contrary, the Zn/GPE/Zn cell showed a stable and consistent low polarization voltage without a potential rise and short circuit. This phenomenon revealed the good compatibility and stability of the gel electrolyte with the zinc anode. Figure 8c displays the voltage-time curves of Zn/GPE/Zn at  $0.5 \text{ mA} \cdot \text{cm}^{-2}$ ,  $1 \text{ mA} \cdot \text{cm}^{-2}$ , and  $1.5 \text{ mA} \cdot \text{cm}^{-2}$ , respectively. Although the polarization voltage increased with the current density, the polarization voltage of GPE was very stable. When the current density decreased to  $0.5 \text{ mA} \cdot \text{cm}^{-2}$  again, the polarization was even more stable than the initial polarization curve. Polarization tests demonstrated the fast electrochemical reaction kinetics under the Zn/GPE/LFP system for rapid stripping/plating of Zn.

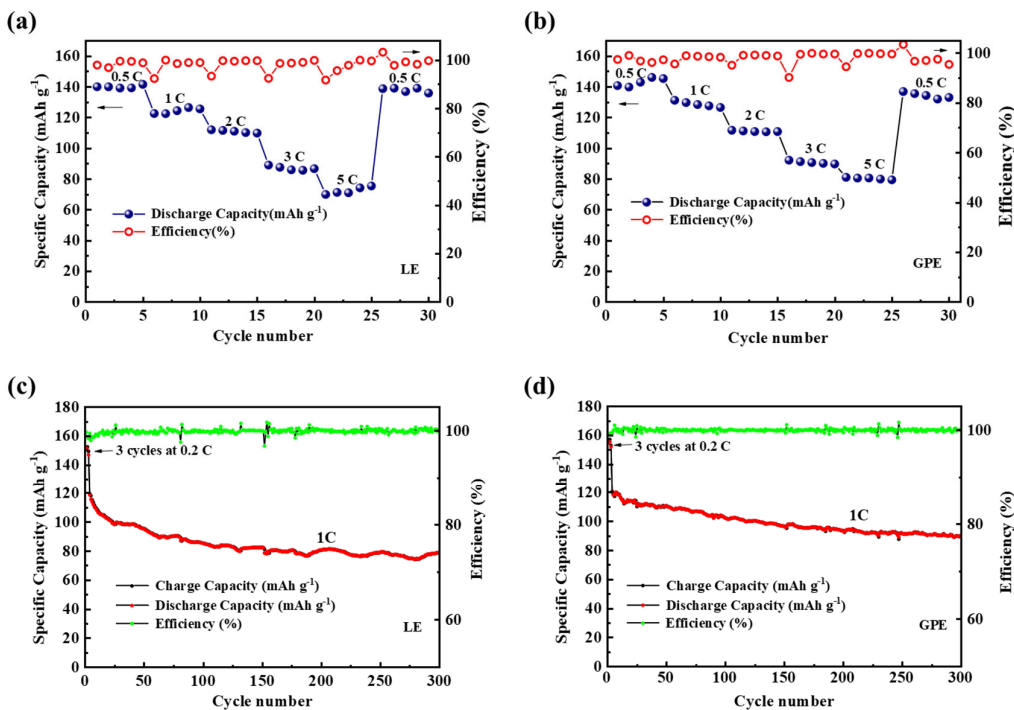


**Figure 7.** Rate capability of (a) Zn/LE/LFP and (b) Zn/GPE/LFP, respectively. Cycle performances and Coulombic efficiency of the (c) Zn/LE/LFP and (d) Zn/GPE/LFP batteries at 1 C.

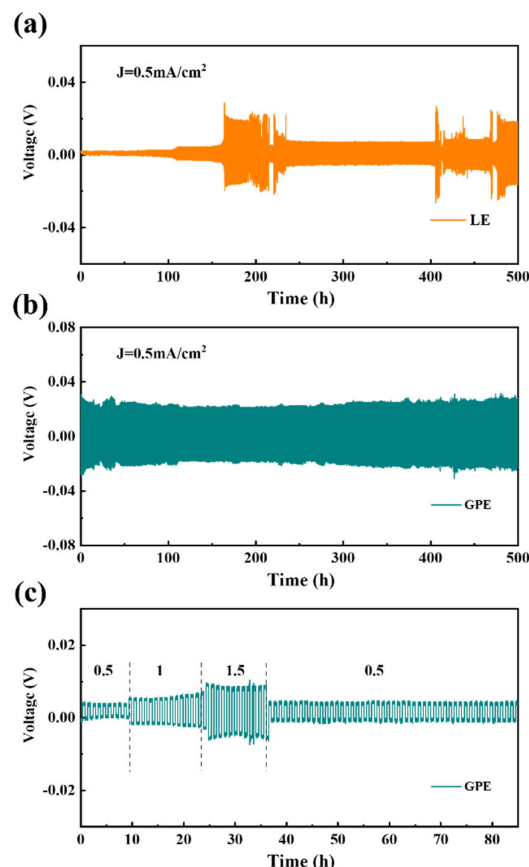


**Figure 8.** Galvanostatic tests of (a) Zn/LE/Zn and (b) Zn/GPE/Zn at  $0.5 \text{ mA} \cdot \text{cm}^{-2}$ , (c) voltage profile of a Zn/GPE/Zn cell under various current densities.

Figure 9a,b show the SEM pictures of the Zn foils after cycling 500 h. It could be observed that after a constant charge/discharge process for 500 h (Figure 9a), the surface of the Zn foil in Zn/LE/Zn was rough and many rod-like materials that should be zinc dendrites were deposited. The zinc dendrites could penetrate the separator and cause short circuits and serious safety problems. From Figure 9b, it can be surveyed that after a 500 h charge/discharge process of constant current, the surface of the Zn foil of Zn/GPE/Zn was smooth without obvious dendrites. Figure 9c explains the deposition mechanism of zinc ions in LE. The zinc ions diffused in a disorderly manner on the zinc anode, and the formation and growth of dendrites led to the diaphragm being punctured. The deposition mechanism of zinc ions in GPE is declared in Figure 9d. On the one hand, the independent pore structure makes a Zn layer uniformly, thus inhibiting the formation of Zn dendrites, and, on the other hand, the robust mechanical properties of GPE further prevented Zn dendrites from penetrating GPE [49]. Therefore, the prepared SiO<sub>2</sub>-SA GPE could enable the zinc anode to obtain better reversibility and stability and improve the electrochemical performance of AZIBs.

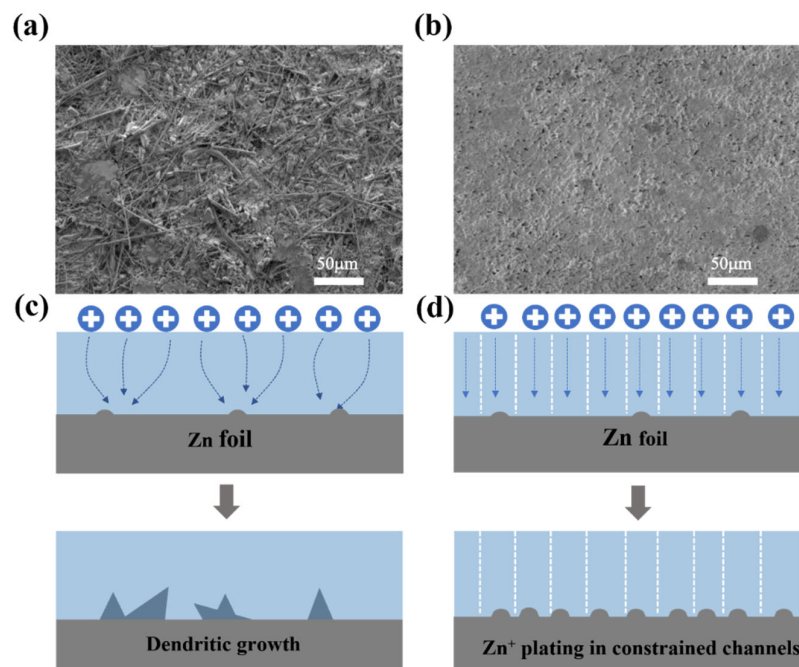


**Figure 9.** The surface morphology of Zn after 500 h in (a) Zn/LE/Zn and (b) Zn/GPE/Zn batteries, respectively. The mechanism for the deposition behaviors of Zn in (c) LE and (d) GPE.

Figure 10a,c show the SEM images of Zn foils in Zn/GPE/LFP batteries. It could be noted that the surface of Zn foil was smooth, and no obvious dendrites were observed, which should be attributed to the stable and uniform Zn stripping/plating. This was sufficient to demonstrate that GPE could significantly inhibit dendrites and reduce the occurrence of a side reaction, resulting in highly reversible and efficient dissolution and deposition of Zn<sup>2+</sup>. In contrast, from Figure 10b,d, zinc dendrites presented obviously on the surface of Zn foil in Zn/LE/LFP, which might be due to the uneven plating/stripping of Zn and a side reaction.

Figure S3 collected the XRD patterns of the anodes in Zn/ /LFP batteries after 300 cycles at 1 C. The new diffraction peaks were found at around (003), (021), and (202) in the Zn foil of LE, manifesting the formation of Zn<sub>5</sub>(OH)<sub>8</sub>Cl<sub>2</sub>·nH<sub>2</sub>O (PDF#07-0155). In sharp contrast, no new diffraction peaks appeared in the zinc foil using GPE, which was consistent with the conclusion of SEM observation and further confirmed that the prepared GPE can effectively inhibit the formation and growth of dendrites, thus improving battery performance. In

addition, compared with other gel electrolytes that have been reported, the prepared GPE showed better performance (Table S1).

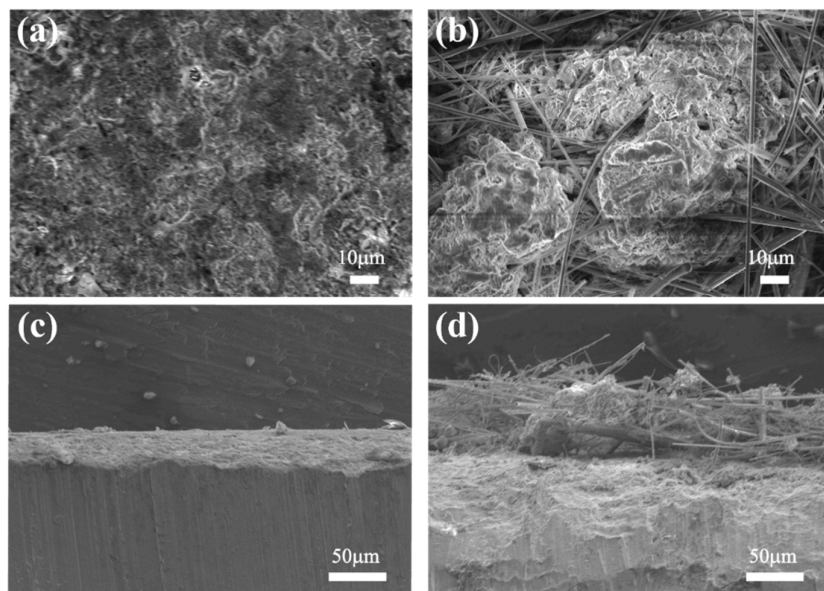


**Figure 10.** The surface morphology of Zn after 300 cycles in (a) Zn/GPE/LFP and (b) Zn/LE/LFP; the cross-sectional morphology of Zn after 300 cycles in (c) Zn/GPE/LFP and (d) Zn/LE/LFP.

#### 4. Conclusions

A SiO<sub>2</sub>-SA gel polymer electrolyte with perfect mechanical strength was prepared through the one-pot method. It revealed stable electrochemical performance after application to aqueous zinc–lithium hybrid batteries. Results illustrated that the SiO<sub>2</sub>-SA GPE had high ionic conductivity of  $1.44 \times 10^{-2}$  S·cm<sup>-1</sup>, excellent flame retardancy, and compatibility with a Zn interface. The zinc ion batteries assembled with SiO<sub>2</sub>-SA GPE could effectively suppress the side effects between electrolyte and electrode, further inhibit the formation and growth of dendrites, and endow the battery with better cycling stability than liquid electrolyte. The capacity retention rate reached 74.9% and the Coulomb efficiency was close to 100% when the zinc batteries cycled 300 turns at 1 C. The SiO<sub>2</sub>-SA GPE displayed excellent electrochemical performance in zinc ion batteries and provided a good electrolyte for the development of solid-state zinc-ion batteries.

**Supplementary Materials:** The following supporting information can be downloaded at: <https://www.mdpi.com/article/10.3390/batteries8100175/s1>; Figure S1: Elastic modulus and toughness of GPE hydrogel matrix; Figure S2: Charge/discharge profiles of (a) Zn/LE/LFP and (b) Zn/GPE/LFP, respectively. Charge/Discharge profiles of (c) Zn/LE/LFP and (d) Zn/GPE/LFP batteries at 3rd, 10th, 50th, 100th, 200th and 300th at the current density of 1 C; cut off voltage 0.9–1.5 V (vs. Zn/Zn<sup>2+</sup>); Figure S3: XRD patterns of the anodes of the Zn//LFP batteries after 300 cycles at 1 C; Table S1: Comparison of the performance of zinc-ion polymer electrolytes.

**Author Contributions:** Investigation and resources P.T. and X.Z.; data curation, C.G.; writing—original draft preparation, P.T.; writing—review and editing, F.S.; supervision, F.S.; project administration, F.S.; funding acquisition, Z.W. and F.S. All authors have read and agreed to the published version of the manuscript.

**Funding:** This research was funded by National Natural Science Foundation of China grant number [22075031] and the Jilin Provincial Science and Technology Development Plan Project [20220101080JC].

**Acknowledgments:** The study was supported by Advanced Institute of Materials Science in Changchun University of Technology.

**Conflicts of Interest:** The authors declare no conflict of interest.

## References

- Placke, T.; Heckmann, A.; Schmuck, R.; Meister, P.; Beltrop, K.; Winter, M. Perspective on Performance, Cost, and Technical Challenges for Practical Dual-Ion Batteries. *Joule* **2018**, *2*, 2528–2550. [[CrossRef](#)]
- Yi, J.; Guo, S.; He, P.; Zhou, H. Status and Prospects of Polymer Electrolytes for Solid-State Li–O<sub>2</sub> (Air) Batteries. *Energy Environ. Sci.* **2017**, *10*, 860–884. [[CrossRef](#)]
- Xue, T.; Fan, H.J. From Aqueous Zn-Ion Battery to Zn-MnO<sub>2</sub> Flow Battery: A Brief Story. *J. Energy Chem.* **2021**, *54*, 194–201. [[CrossRef](#)]
- Yi, J.; Liu, X.; Liang, P.; Wu, K.; Xu, J.; Liu, Y.; Zhang, J. Non-Noble Iron Group (Fe, Co, Ni)-Based Oxide Electrocatalysts for Aqueous Zinc–Air Batteries: Recent Progress, Challenges, and Perspectives. *Organometallics* **2018**, *38*, 1186–1199. [[CrossRef](#)]
- Cui, J.; Liu, X.; Xie, Y.; Wu, K.; Wang, Y.; Liu, Y.; Zhang, J.; Yi, J.; Xia, Y. Improved Electrochemical Reversibility of Zn Plating/Stripping: A Promising Approach to Suppress Water-Induced Issues through the Formation of H-Bonding. *Mater. Today Energy* **2020**, *18*, 100563. [[CrossRef](#)]
- Gao, J.; Zhao, Y.-S.; Shi, S.-Q.; Li, H. Lithium-Ion Transport in Inorganic Solid State Electrolyte. *Chin. Phys. B* **2016**, *25*, 018211. [[CrossRef](#)]
- Xing, L.; Zheng, X.; Schroeder, M.; Alvarado, J.; von Wald Cresce, A.; Xu, K.; Li, Q.; Li, W. Deciphering the Ethylene Carbonate–Propylene Carbonate Mystery in Li-Ion Batteries. *Acc. Chem. Res.* **2018**, *51*, 282–289. [[CrossRef](#)] [[PubMed](#)]
- Mo, R.; Tan, X.; Li, F.; Tao, R.; Xu, J.; Kong, D.; Wang, Z.; Xu, B.; Wang, X.; Wang, C.; et al. Tin-Graphene Tubes as Anodes for Lithium-Ion Batteries with High Volumetric and Gravimetric Energy Densities. *Nat. Commun.* **2020**, *11*, 1374. [[CrossRef](#)]
- Praveen, S.; Santhoshkumar, P.; Joe, Y.C.; Senthil, C.; Lee, C.W. 3D-Printed Architecture of Li-Ion Batteries and Its Applications to Smart Wearable Electronic Devices. *Appl. Mater. Today* **2020**, *20*, 100688. [[CrossRef](#)]
- Li, N.; Chen, H.; Yang, S.; Yang, H.; Jiao, S.; Song, W.L. Bidirectional Planar Flexible Snake-Origami Batteries. *Adv. Sci.* **2021**, *8*, e2101372. [[CrossRef](#)] [[PubMed](#)]
- Xu, Y.; Shen, W.; Wang, C.; Zhang, A.; Xu, Q.; Liu, H.; Wang, Y.; Xia, Y. Hydrothermal Synthesis and Electrochemical Performance of Nanoparticle Li<sub>2</sub>FeSiO<sub>4</sub>/C Cathode Materials for Lithium Ion Batteries. *Electrochim. Acta* **2015**, *167*, 340–347. [[CrossRef](#)]
- Kim, H.; Hong, J.; Park, K.Y.; Kim, H.; Kim, S.W.; Kang, K. Aqueous Rechargeable Li and Na Ion Batteries. *Chem. Rev.* **2014**, *114*, 11788–11827. [[CrossRef](#)]
- Fang, G.; Zhu, C.; Chen, M.; Zhou, J.; Tang, B.; Cao, X.; Zheng, X.; Pan, A.; Liang, S. Suppressing Manganese Dissolution in Potassium Manganate with Rich Oxygen Defects Engaged High-Energy-Density and Durable Aqueous Zinc-Ion Battery. *Adv. Funct. Mater.* **2019**, *29*, 1808375. [[CrossRef](#)]
- Liu, F.; Chen, Z.; Fang, G.; Wang, Z.; Cai, Y.; Tang, B.; Zhou, J.; Liang, S. V<sub>2</sub>O<sub>5</sub> Nanospheres with Mixed Vanadium Valences as High Electrochemically Active Aqueous Zinc-Ion Battery Cathode. *Nano Micro Lett.* **2019**, *11*, 25. [[CrossRef](#)]
- Yang, D.; Tan, H.; Rui, X.; Yu, Y. Electrode Materials for Rechargeable Zinc-Ion and Zinc-Air Batteries: Current Status and Future Perspectives. *Electrochem. Energy Rev.* **2019**, *2*, 395–427. [[CrossRef](#)]
- Yang, Y.; Tang, Y.; Fang, G.; Shan, L.; Guo, J.; Zhang, W.; Wang, C.; Wang, L.; Zhou, J.; Liang, S. Li<sup>+</sup> Intercalated V<sub>2</sub>O<sub>5</sub>·nH<sub>2</sub>O with Enlarged Layer Spacing and Fast Ion Diffusion as an Aqueous Zinc-Ion Battery Cathode. *Energy Environ. Sci.* **2018**, *11*, 3157–3162. [[CrossRef](#)]
- Zhang, X.; Wang, L.; Fu, H. Recent Advances in Rechargeable Zn-Based Batteries. *J. Power Sources* **2021**, *493*, 229677. [[CrossRef](#)]
- Zhao, Y.; Zhu, Y.; Zhang, X. Challenges and Perspectives for Manganese-Based Oxides for Advanced Aqueous Zinc-Ion Batteries. *InfoMat* **2019**, *2*, 237–260. [[CrossRef](#)]
- Huang, S.; Zhu, J.; Tian, J.; Niu, Z. Recent Progress in the Electrolytes of Aqueous Zinc-Ion Batteries. *Chem. A Eur. J.* **2019**, *25*, 14480–14494. [[CrossRef](#)] [[PubMed](#)]
- Naveed, A.; Yang, H.; Shao, Y.; Yang, J.; Yanna, N.; Liu, J.; Shi, S.; Zhang, L.; Ye, A.; He, B.; et al. A Highly Reversible Zn Anode with Intrinsically Safe Organic Electrolyte for Long-Cycle-Life Batteries. *Adv. Mater.* **2019**, *31*, 1900668. [[CrossRef](#)]
- Naveed, A.; Yang, H.; Yang, J.; Nuli, Y.; Wang, J. Highly Reversible and Rechargeable Safe Zn Batteries Based on a Triethyl Phosphate Electrolyte. *Angew. Chem. Int. Ed.* **2019**, *58*, 2760–2764. [[CrossRef](#)]
- Han, C.; Wang, X.; Peng, J.; Xia, Q.; Chou, S.; Cheng, G.; Huang, Z.; Li, W. Recent Progress on Two-Dimensional Carbon Materials for Emerging Post-Lithium (Na<sup>+</sup>, K<sup>+</sup>, Zn<sup>2+</sup>) Hybrid Supercapacitors. *Polymers* **2021**, *13*, 2137. [[CrossRef](#)]
- Hao, J.; Li, X.; Zeng, X.; Li, D.; Mao, J.; Guo, Z. Deeply Understanding the Zn Anode Behaviour and Corresponding Improvement Strategies in Different Aqueous Zn-Based Batteries. *Energy Environ. Sci.* **2020**, *13*, 3917–3949. [[CrossRef](#)]
- Zhang, Q.; Luan, J.; Tang, Y.; Ji, X.; Wang, H. Interfacial Design of Dendrite-Free Zinc Anodes for Aqueous Zinc-Ion Batteries. *Angew. Chem. Int. Ed.* **2020**, *59*, 13180–13191. [[CrossRef](#)]
- Wu, K.; Huang, J.; Yi, J.; Liu, X.; Liu, Y.; Wang, Y.; Zhang, J.; Xia, Y. Recent Advances in Polymer Electrolytes for Zinc Ion Batteries: Mechanisms, Properties, and Perspectives. *Adv. Energy Mater.* **2020**, *10*, 1903977. [[CrossRef](#)]
- Ruiz-Martínez, D.; Kovacs, A.; Gómez, R. Development of Novel Inorganic Electrolytes for Room Temperature Rechargeable Sodium Metal Batteries. *Energy Environ. Sci.* **2017**, *10*, 1936–1941. [[CrossRef](#)]
- Mo, F.; Liang, G.; Wang, D.; Tang, Z.; Li, H.; Zhi, C. Biomimetic Organohydrogel Electrolytes for High-Environmental Adaptive Energy Storage Devices. *EcoMat* **2019**, *1*, e12008. [[CrossRef](#)]
- Wang, Z.; Ruan, Z.; Liu, Z.; Wang, Y.; Tang, Z.; Li, H.; Zhu, M.; Hung, T.F.; Liu, J.; Shi, Z.; et al. A Flexible Rechargeable Zinc-Ion Wire-Shaped Battery with Shape Memory Function. *J. Mater. Chem. A* **2018**, *6*, 8549–8557. [[CrossRef](#)]

29. Tang, Y.; Liu, C.; Zhu, H.; Xie, X.; Gao, J.; Deng, C.; Han, M.; Liang, S.; Zhou, J. Ion-Confinement Effect Enabled by Gel Electrolyte for Highly Reversible Dendrite-Free Zinc Metal Anode. *Energy Storage Mater.* **2020**, *27*, 109–116. [[CrossRef](#)]
30. Huang, J.; Chi, X.; Yang, J.; Liu, Y. An Ultrastable Na-Zn Solid-State Hybrid Battery Enabled by a Robust Dual-Cross-Linked Polymer Electrolyte. *ACS Appl. Mater. Interfaces* **2020**, *12*, 17583–17591. [[CrossRef](#)]
31. Ding, F.; Xu, W.; Graff, G.L.; Zhang, J.; Sushko, M.L.; Chen, X.; Shao, Y.; Engelhard, M.H.; Nie, Z.; Xiao, J.; et al. Dendrite-Free Lithium Deposition Via Self-Healing Electrostatic Shield Mechanism. *J. Am. Chem. Soc.* **2013**, *135*, 4450–4456. [[CrossRef](#)] [[PubMed](#)]
32. Han, Q.; Chi, X.; Zhang, S.; Liu, Y.; Zhou, B.; Yang, J.; Liu, Y. Durable, Flexible Self-Standing Hydrogel Electrolytes Enabling High-Safety Rechargeable Solid-State Zinc Metal Batteries. *J. Mater. Chem. A* **2018**, *6*, 23046–23054. [[CrossRef](#)]
33. Zhu, R.; Yang, H.; Cui, W.; Fadillah, L.; Huang, T.; Xiong, Z.; Tang, C.; Kowalski, D.; Kitano, S.; Zhu, C.; et al. High Strength Hydrogels Enable Dendrite-Free Zn Metal Anodes and High-Capacity Zn-MnO<sub>2</sub> Batteries Via a Modified Mechanical Suppression Effect. *J. Mater. Chem. A* **2022**, *10*, 3122–3133. [[CrossRef](#)]
34. Ding, Y.; Zhong, X.; Yuan, C.; Duan, L.; Zhang, L.; Wang, Z.; Wang, C.; Shi, F. Sodium Alginate Binders for Bivalence Aqueous Batteries. *ACS Appl. Mater. Interfaces* **2021**, *13*, 20681–20688. [[CrossRef](#)]
35. Yuan, C.; Zhong, X.; Tian, P.; Wang, Z.; Gao, G.; Duan, L.; Wang, C.; Shi, F. Antifreezing Zwitterionic-Based Hydrogel Electrolyte for Aqueous Zn Ion Batteries. *ACS Appl. Energy Mater.* **2022**, *5*, 7530–7537. [[CrossRef](#)]
36. Pirzada, T.; Arvidson, S.A.; Saquing, C.D.; Shah, S.S.; Khan, S.A. Hybrid Silica-Pva Nanofibers Via Sol-Gel Electrospinning. *Langmuir* **2012**, *28*, 5834–5844. [[CrossRef](#)]
37. Hou, Y.; Zhong, X.; Ding, Y.; Zhang, S.; Shi, F.; Hu, J. Alginate-Based Aerogels with Double Catalytic Activity Sites and High Mechanical Strength. *Carbohydr. Polym.* **2020**, *245*, 116490. [[CrossRef](#)]
38. Liu, Y.; Zhao, X.-R.; Peng, Y.-L.; Wang, D.; Yang, L.; Peng, H.; Zhu, P.; Wang, D.-Y. Effect of Reactive Time on Flame Retardancy and Thermal Degradation Behavior of Bio-Based Zinc Alginate Film. *Polym. Degrad. Stab.* **2016**, *127*, 20–31. [[CrossRef](#)]
39. Li, H.; Liu, Z.; Liang, G.; Huang, Y.; Huang, Y.; Zhu, M.; Pei, Z.; Xue, Q.; Tang, Z.; Wang, Y.; et al. Waterproof and Tailorable Elastic Rechargeable Yarn Zinc Ion Batteries by a Cross-Linked Polyacrylamide Electrolyte. *ACS Nano* **2018**, *12*, 3140–3148. [[CrossRef](#)]
40. Karapanagiotis, I.; Manoudis, P.N.; Zurba, A.; Lampakis, D. From Hydrophobic to Superhydrophobic and Superhydrophilic Siloxanes by Thermal Treatment. *Langmuir* **2014**, *30*, 13235–13243. [[CrossRef](#)]
41. Chen, M.; Chen, J.; Zhou, W.; Han, X.; Yao, Y.; Wong, C.P. Realizing an All-Round Hydrogel Electrolyte toward Environmentally Adaptive Dendrite-Free Aqueous Zn-MnO<sub>2</sub> Batteries. *Adv. Mater.* **2021**, *33*, e2007559. [[CrossRef](#)] [[PubMed](#)]
42. Yang, Q.; Mo, F.; Liu, Z.; Ma, L.; Li, X.; Fang, D.; Chen, S.; Zhang, S.; Zhi, C. Activating C-Coordinated Iron of Iron Hexacyanoferrate for Zn Hybrid-Ion Batteries with 10 000-Cycle Lifespan and Superior Rate Capability. *Adv. Mater.* **2019**, *31*, e1901521. [[CrossRef](#)] [[PubMed](#)]
43. Zhang, Q.; Ma, Y.; Lu, Y.; Li, L.; Wan, F.; Zhang, K.; Chen, J. Modulating Electrolyte Structure for Ultralow Temperature Aqueous Zinc Batteries. *Nat. Commun.* **2020**, *11*, 4463. [[CrossRef](#)]
44. Zhu, M.; Wang, X.; Tang, H.; Wang, J.; Hao, Q.; Liu, L.; Li, Y.; Zhang, K.; Schmidt, O.G. Antifreezing Hydrogel with High Zinc Reversibility for Flexible and Durable Aqueous Batteries by Cooperative Hydrated Cations. *Adv. Funct. Mater.* **2019**, *30*, 1907218. [[CrossRef](#)]
45. Hong, Z.; Ahmad, Z.; Viswanathan, V. Design Principles for Dendrite Suppression with Porous Polymer/Aqueous Solution Hybrid Electrolyte for Zn Metal Anodes. *ACS Energy Lett.* **2020**, *5*, 2466–2474. [[CrossRef](#)]
46. Zeng, Y.; Zhang, X.; Meng, Y.; Yu, M.; Yi, J.; Wu, Y.; Lu, X.; Tong, Y. Achieving Ultrahigh Energy Density and Long Durability in a Flexible Rechargeable Quasi-Solid-State Zn-MnO<sub>2</sub> Battery. *Adv. Mater.* **2017**, *29*, 1700274. [[CrossRef](#)]
47. Huang, Y.; Zhang, J.; Liu, J.; Li, Z.; Jin, S.; Li, Z.; Zhang, S.; Zhou, H. Flexible and Stable Quasi-Solid-State Zinc Ion Battery with Conductive Guar Gum Electrolyte. *Mater. Today Energy* **2019**, *14*, 100349. [[CrossRef](#)]
48. Turković, A.; Pavlović, M.; Dubček, P.; Lučić-Lavčević, M.; Etlinger, B.; Bernstorff, S. SAXS/DSC Study of Polymer Electrolyte for Zn Rechargeable Nanostructured Galvanic Cells. *J. Electrochem. Soc.* **2007**, *154*, A554. [[CrossRef](#)]
49. Karger-Kocsis, J.; Keki, S. Biodegradable Polyester-Based Shape Memory Polymers: Concepts of (Supra)Molecular Architecturing. *Express Polym. Lett.* **2014**, *8*, 397–412. [[CrossRef](#)]